Structure, electronic properties, and energetics of oxygen vacancies in varying concentrations of $Si_xGe_{1-x}O_2$

Al-Moatasem El-Sayed,[1,2,*] Markus Jech,[1,†] Dominic Waldhör,[1,‡] Alexander Makarov,[1,3,§] Mikhail I. Vexler,[4,∥] and Stanislav Tyaginov[3,4,¶]

[1]Institute for Microelectronics, Technische Universität Wien, A-1040 Vienna, Austria
[2]Nanolayers Research Computing, Ltd., 1 Granville Court, Granville Road, London N12 0HL, United Kingdom
[3]imec, Leuven 3001, Belgium
[4]A.F. Ioffe Physical-Technical Institute, 194021 St.-Petersburg, Russia

(Received 23 November 2021; accepted 2 November 2022; published 5 December 2022)

SiGe alloys, widely used in various technological applications, are typically interfaced with a thermally grown oxide layer that is composed of $Si_xGe_{1-x}O_2$, a composite material which is also used for technological applications in its own right. Point defects in this oxide layer influence the electronic and structural properties, which can detrimentally affect the desired application. In this paper, we use *ab initio* calculations to investigate the canonical oxygen vacancy in systems of varying compositions of $Si_xGe_{1-x}O_2$. We find that the electronic structures and geometries of the vacancies remain qualitatively similar to their well-known analogs in SiO_2 and GeO_2 regardless of the composition and similar to previous results in the literature on Ge-doped SiO_2. They show a wide distribution of formation energies and one-electron levels across the various concentrations of $Si_xGe_{1-x}O_2$. However, our results show that the factor defining their quantitative behavior is not the concentration, rather it is the chemistry of the atoms around the vacancy, each combination of which has its own distribution of properties. The resulting charge transition levels similarly cover a wide range of the band gap. These results aid the understanding of reliability issues in technological applications.

DOI: 10.1103/PhysRevMaterials.6.125002

I. INTRODUCTION

Silicon forms the basis of an immense range of technologies due to its abundance, electronic and optical properties, and the stability of its native oxide [1–7]. The continuous miniaturization of Si-based electronic devices, now approaching its physical limits, has led researchers to explore alternative material combinations. The ability to change and regulate optical properties in mixed SiGe systems has led to investigations of alternative material systems. Combining Si and Ge allows one to modify and fine tune the material's properties, opening up a wider range of possible applications [8].

In these applications, the effects of point defects can significantly alter the material's expected behavior. For example, in electronic devices, recent atomistic simulations provided insight into the mechanisms of Si-H dissociation leading to a point defect that causes reliability issues [9,10]. A further example comes from the fabrication of optical fibers, where germanosilicate glasses of the form $Si_xGe_{1-x}O_2$ are widely used [6,7,11,12]. In Ge-doped silica fibers, defects lead to radiation-induced attenuation that is pronounced in the UV range [7]. This attenuation is thought to be caused by Ge-related defects rather than Si and could be related to the oxygen vacancy. With the presence of varying concentrations of Ge in novel devices and applications, understanding how oxygen vacancies behave in varying concentrations of $Si_xGe_{1-x}O_2$ can help to assess their role in detrimental issues [13–15].

On a more fundamental level, atomistic simulations have provided great insight into the behavior of vacancies in pure amorphous (a-) SiO_2 and a-GeO_2. The oxygen vacancy, which was discovered experimentally in the 1950s, is a prototypical defect in both SiO_2 and GeO_2 [16–19]. Calculations show that the neutral vacancy can be found in crystalline (c) and amorphous (a) a-SiO_2 and consists of an Si-Si dimer, with a bond length of around 2.4 Å depending on the method used [20–22]. It consists of a fully occupied bonding orbital and an empty antibonding orbital. It can therefore go on to capture either a hole or an electron to form a positively or negatively charged state. The positively charged state in both c- and a-SiO_2 consists of two metastable states, typically denoted as the dimer and the puckered configuration in the literature [23–28]. They are correlated with the E'_δ and the E'_γ signals measured by electronic paramagnetic resonance [29]. The E'_δ (dimer configuration) has been characterized as a slightly extended Si-Si bond due to the lack of an electron in its bonding orbital. In contrast, the E'_γ (puckered configuration) is a 3-coordinated Si with a single electron in a dangling bond facing a positively charged Si atom that relaxes through the plane

*elsayed@iue.tuwien.ac.at
†jech@iue.tuwien.ac.at
‡waldhoer@iue.tuwien.ac.at
§alexander.makarov@imec.be
∥vexler@mail.ioffe.ru
¶stanislav.tyaginov@imec.be

 ©2022 American Physical Society

of its oxygen neighbors to interact with an O atom that sits nearby. In c-SiO_2, the puckered configuration is more stable, while in a-SiO_2, it depends on the location in the matrix where it is formed [27]. In GeO_2, the vacancy behaves quite similar to SiO_2 [30–32]. However, they can undergo conversion reactions, resulting in the formation of other experimentally measured defects [33]. Calculations made on Ge-doped (2.8% mol) SiO_2 show that the oxygen vacancy behaves similar to its analog in pure a-SiO_2 and a-GeO_2, with quantitative variations in its geometry and electronic structure [34]. The vacancies in Ge-doped SiO_2 were shown to have a lower formation energy when formed from an initial Ge-O-Si moiety along with slightly longer average bond lengths. However, a systematic analysis of the behavior of oxygen vacancies in varying compositions of $Si_xGe_{1-x}O_2$ is still lacking.

Here, we use *ab initio* calculations to build upon previous simulations in the literature and systematically explore a canonical defect, the oxygen vacancy, in $Si_xGe_{1-x}O_2$ with varying values of x. The well-known defect in both crystalline and amorphous SiO_2 is characterized by the lack of an O atom between two Si atoms [27,28,31,35]. We show that the vacancy persists across all concentrations of $Si_xGe_{1-x}O_2$ with a qualitatively similar geometrical structure. It is able to trap both positive and negative charges as in a-SiO_2 [27,35]. At a first glance, the defects' atomic and electronic structures appear to vary widely as x changes in $Si_xGe_{1-x}O_2$; however, we show that its properties primarily depend on the atom types involved in the vacancy. Their formation energies were calculated in all three charge states and shown to mainly depend on the surrounding atoms and the distance between them, with vacancies surrounded by two Ge atoms tending to be lower in energy. The thermodynamic charge transition levels were calculated and shown to cover a large section of the $Si_xGe_{1-x}O_2$ band gap. Unlike the a-SiO_2 vacancy, those in $Si_xGe_{1-x}O_2$ have Kohn-Sham levels and charge transition levels that sit further away from the $Si_xGe_{1-x}O_2$ valence band and would, therefore, sit closer to the band edges of the Si or SiGe substrate when used as a gate dielectric in electronic device applications. These results suggest that the O vacancy could play a more substantial role in electronic device reliability issues and optical device design due to its wide range of properties.

II. METHODS OF CALCULATIONS

In this paper, oxygen vacancies in $Si_xGe_{1-x}O_2$ systems were studied using density functional theory (DFT). In order to prepare the mixed $Si_xGe_{1-x}O_2$ systems, we start from a periodic cell of a-SiO_2 containing 216 atoms prepared using a melt-and-quench method [36]. In order to remove any residual strain in the model structures, the cell vectors were optimized. We note that due to the small sample size relative to the long-range order of the amorphous material, the resulting cells are not exactly orthorhombic, with the angle between cell vectors varying between 89.5° and 91.5°. To create varying concentrations of $Si_xGe_{1-x}O_2$, Si atoms were replaced by the appropriate number of Ge atoms followed by an optimization of the cell vectors. One cell each consisting of concentrations of 0%, 25%, 50%, and 100% Si were used in this study.

Models of a-SiO_2 were used as a starting point since the structure of a-SiO_2 and a-GeO_2 have been shown to be qualitatively similar [37]. However, certain aspects of the structure cannot be described using this approach; for example, the increased concentration of three-membered rings in a-GeO_2 compared to the original a-SiO_2 structure that was used [37]. This should have a small quantitative effect on the results, as the local and medium structure—described by the bond lengths and angles as well as the structure factors—is still well described in our approach. For each concentration studied, a vacancy was created at each possible site by removing an oxygen atom. This resulted in 144 configurations of the vacancy for each concentration of $Si_xGe_{1-x}O_2$. An O atom is bound to two cations. We classify the vacancy here by the chemical identity of the two atoms that were bound to the O before it was removed. For example, an O atom bound to one Si and one Ge atom would lead to an Si-Ge-type vacancy upon the removal of the O.

The geometric and electronic properties of vacancies in $Si_xGe_{1-x}O_2$ were calculated using DFT as implemented in the CP2K code [38]. All calculations were sampled at the Γ point only and used the Gaussian plane-wave (GPW) method [39]. Both a Gaussian and a plane-wave basis set were therefore used to describe the Kohn-Sham orbitals and the resulting electron density. The plane-wave cutoff in these calculations was set to $17.7\ \times 10^3$ eV (1300 Ry), as the total energy was clearly converged at that point in both SiO_2 and GeO_2 systems. The Gaussian basis sets used to describe Si, Ge, and O atoms are the double-ζ basis sets, which are known in the CP2K code as the molecular optimized (MOLOPT) basis sets [40]. Goedecker-Tetter-Hutter (GTH) pseudopotentials were used to describe the core electrons of all the atoms. Exchange and correlation were calculated using the hybrid, long-range corrected Perdew-Burke-Ernzerhof Truncated Coulomb Long-range Corrected (PBE0_TC_LRC) functional with the Coulomb operator truncated to a radius of 2 Å and a 25% proportion of Hartree-Fock exchange (HFX) [41]. To mitigate the expense of calculating the integrals required for the HFX, the auxiliary density matrix method (ADMM) was used [42]. It assumes that the difference in calculating HFX on two basis sets, one of which is smaller and faster converging, is approximately the same as the difference in exchange calculated at the PBE level. Adding this difference to the HFX calculated on the smaller, auxiliary basis set results in a good estimation of the HFX in the full basis set. In our test calculations on a cell of a-SiO_2 containing 216 atoms, the difference in HFX using the full basis set and the ADMM method was of the order of 10 meV. The auxiliary basis sets used for all atoms are known as pFIT3 in the CP2K code. The electronic structures were converged to within a tolerance of 3×10^{-6} eV. All cell and geometry optimizations were performed using the Broyden-Fletcher-Goldfarb-Shanno (BFGS) algorithm to minimize forces on atoms and the cell to within 37 pN (2.3×10^{-2} eV Å^{-1}).

To characterize the thermodynamic properties of the defect, the formation energy was approximated as [43]

$$E_{\text{for}}(\epsilon_{\text{F}}, q) = E_{\text{defect}}(q) - (E_{\text{bulk}} + \mu_{\text{O}}) + q(\epsilon_{\text{F}} + \Delta V) + E_{\text{corr}}, \quad (1)$$

where $E_{\text{defect}}(q)$ is the total energy of the defective system in charge state q, E_{bulk} is the total energy of the defect-free system, μ_{O} is the chemical potential of an O atom calculated using the same method, ϵ_{F} is the Fermi level referenced to the top of the $Si_xGe_{1-x}O_2$ valence band, ΔV is a potential alignment term, and E_{corr} is a correction term for the periodic interaction between localized charges in charged systems. In order to calculate the chemical potential of the O atom, we used half of the energy of an oxygen molecule in a cell with fixed boundary conditions; it effectively describes the chemical potential of O in an O-rich environment and inevitably includes the binding energy of the molecule. The ΔV term was found to be negligible (<0.05 eV) in our systems and was therefore ignored. We used the method proposed by Lany and Zunger to calculate the charge correction. This was due to its ability to describe the interaction between a localized charge and extended delocalized screening charge density [44,45]. The correction was calculated for each cell as

$$E_{\text{corr}} = \left[1 - \frac{\pi}{3\alpha}\left(1 - \frac{1}{\varepsilon}\right)\right]\frac{q^2\alpha}{2\varepsilon L}, \tag{2}$$

where ε is the macroscopic dielectric constant of the material, q is the charge of the cell, α is the Madelung constant for a single charge in a periodic array, and L is the supercell length. As our cells are very close to being numerically orthorombic, we use an arithmetic average of the magnitude of the cell vectors, which varied by 2% at most. As an estimate for the dielectric constant of the varying compositions, we interpolate linearly from its experimental values between a-SiO_2 (3.9) and a-GeO_2 (5.9). We note that the correction used here is similar in magnitude to the Freyholdt, Neugebauer, and Van de Walle correction [45,46] and is similar to results seen in the literature for defects in crystalline materials [47].

III. RESULTS

We begin by characterizing our $Si_xGe_{1-x}O_2$ samples. The structural and electronic properties of both a-SiO_2 and a-GeO_2 have been studied very well over the past few decades, both experimentally and theoretically. It has a band gap of around 8.9 eV with the top of the valence band being mostly composed of O nonbonding p and the bottom of the conduction band being made of Si d states. The electronic structure of a-GeO_2 is very similar, but with the bottom of the conduction band being composed of Ge d states and a reduced band gap of ≈5.6 eV. Our calculations confirm this qualitative behavior, but the calculated band gaps for a-SiO_2 and a-GeO_2 are slightly underestimated compared to the experimental values in the literature. Adjusting the amount of HFX exchange can be used to obtain a more accurate band gap compared to experiment; however, the standard formulation of the PBE0_TC_LRC functional was used throughout this work to ensure the comparability of the results across all structures. The band gap was calculated as the difference between the energies of the highest occupied and lowest unoccupied states. In pure a-GeO_2, the calculated band gap was 5.50 eV, while that of a-SiO_2 was 8.22 eV, as can be seen in Table I. As the Si concentration was changed, the system's electronic structure remained qualitatively the same as described above, with quantitative differences summarized in Table I.

TABLE I. Structural and electronic properties of the simulated $Si_xGe_{1-x}O_2$ cells. The concentration indicates the number percentage of Si atoms. Ge-O and Si-O indicate the respective bond lengths with their standard deviations, σ, both of which are measured in Å. ρ is the cell density measured in g cm^{-3} and E_g indicates the band gap which was measured in eV.

Concentration	Ge-O	σ(Ge-O)	Si-O	σ(Si-O)	ρ	E_g
0%	1.744	0.010	N/A	N/A	3.37	5.50
25%	1.742	0.011	1.615	0.0099	3.08	5.79
50%	1.741	0.013	1.615	0.010	2.83	6.17
75%	1.736	0.014	1.614	0.012	2.52	6.64
100%	N/A	N/A	1.613	0.013	2.20	8.22

We note that there is a large drop in band gap on going from 100% to 75% Si that has also been reported in previous calculations [48]. This can be explained as a transition from a molecular orbital picture to a band theory view. Considering that a-SiO_2 has a larger band gap than a-GeO_2, adding a single Ge atom to pure a-SiO_2 introduces localized molecular orbitals, including an antibonding orbital, that sit below the a-SiO_2 band gap. As the concentration of Ge atoms increases, a band begins to form whose dispersion increases with the number of added Ge atoms. Therefore, the initial introduction of Ge appears as a large drop in the band gap due to the energetically lower Ge antibonding states. This band's width increases more slowly than the initial drop and explains why the band gap changes less drastically between 75% to 0% Si atoms. The densities of states of the various concentrations are included in Fig. 1 of the Supplemental Material and show this effect [49]. Indeed, visualizing the lowest unoccupied states in the 75% Ge system shows that it is partially localized mainly over the Ge atoms (see Fig. 2 of the Supplemental Material [49]). The oxygen states that make up the top of the valence band are qualitatively rather similar regardless of whether it has Si or Ge neighbors. As the concentration of Si increases, however, the O atoms bound to Ge tend to have deeper states in the valence band (see Fig. 1 in the Supplemental Material [49]).

In pure a-GeO_2 models, the average Ge-O bond length was calculated as 1.74 Å, while the average Si-O bond length is relatively shorter, averaging at 1.61 Å in pure a-SiO_2. Both bond lengths have very small standard deviations which do not exceed 0.02 Å. Changing the concentration of the $Si_xGe_{1-x}O_2$ system affects these bond lengths in similar ways. As the concentration of Si increases, the Si-O bond length shortens until it reaches its equilibrium length in pure a-SiO_2, while the Ge-O bond length shows the opposite behavior. One can view this as the bond length being modified by the dominating species in the system. However, we note that these changes in bond length are relatively very small. The larger Ge-O bond length results in the cell volume increasing as the Ge content increases; however, due to the much higher mass of Ge, the density of the system increases. The range of densities reported in Table I is very similar to the 2.17 to 3.63 g cm^{-3} reported in the literature [32,48].

To quantify the long-range order, the total structure factors of the studied systems were calculated, as depicted in Fig. 1.

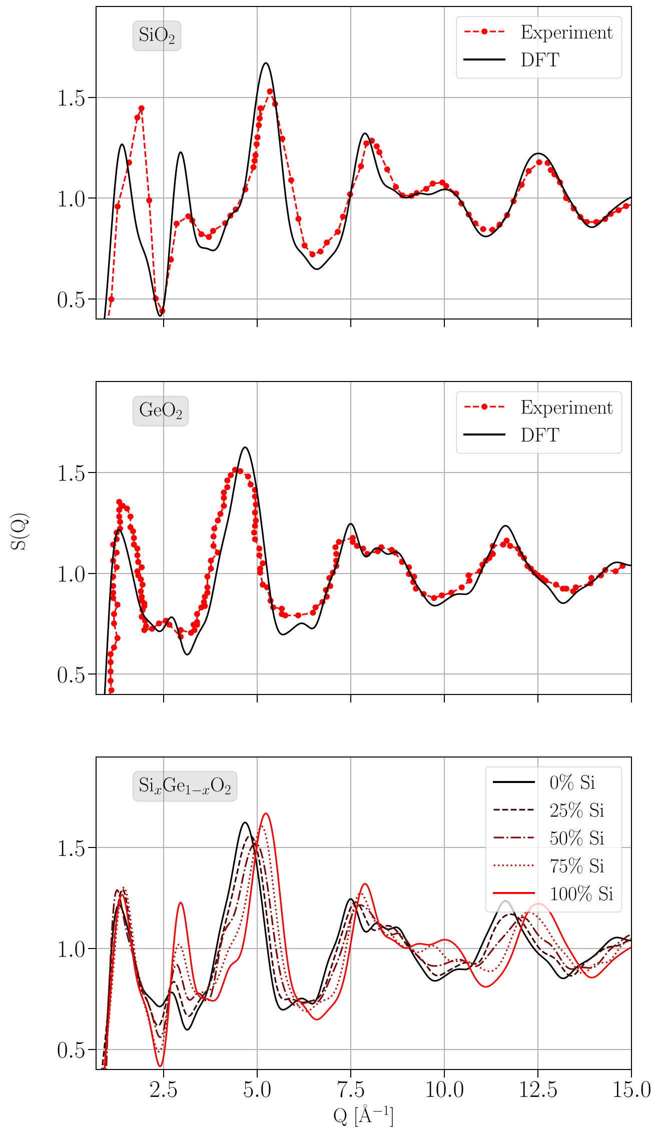

FIG. 1. Total neutron structure factors of a-SiO_2 (top panel) and a-GeO_2 (middle panel) compared to experiment [37]. The black solid lines are the results from the calculated models, while the red markers with dashed lines are data points from experiment. The bottom panel shows the simulated structure factors for all concentrations of $Si_xGe_{1-x}O_2$ considered in this paper which show a smooth transition from the structure factor of a-GeO_2 to a-SiO_2.

For pure a-SiO_2 and a-GeO_2, experimental structure factors have been measured in the literature [37]. Comparing the simulated models to experiment in the top two panels of Fig. 1, it can clearly be seen that they closely match each other, giving confidence that the structures are indeed representative of the materials. The bottom panel of Fig. 1 shows the structure factors of the various concentrations of $Si_xGe_{1-x}O_2$. One can see a smooth transition between the structure factors of the pure materials as the concentration of the $Si_xGe_{1-x}O_2$ varies.

Oxygen vacancies in $Si_xGe_{1-x}O_2$

To model oxygen vacancies in $Si_xGe_{1-x}O_2$, one oxygen atom was removed from the defect-free systems described in the previous section followed by a minimization of the system's total energy with respect to its atomic coordinates. For each $Si_xGe_{1-x}O_2$ concentration that was modeled, the O vacancy was introduced at all 144 possible sites. Each vacancy can trap one hole or electron; therefore, all vacancies were modeled in their neutral, positive, and negative charge states. Here, we describe their structural and electronic properties in these different charge states and in $Si_xGe_{1-x}O_2$ with varying concentrations of x. We note here that since the behavior of the defects is described by the chemical identity of the atoms surrounding the vacancy, and to make the text more concise, *a list of three consecutive numbers highlighted in italics refers to vacancies with Ge-Ge, Si–Si, and Si-Ge neighbors, in that order*.

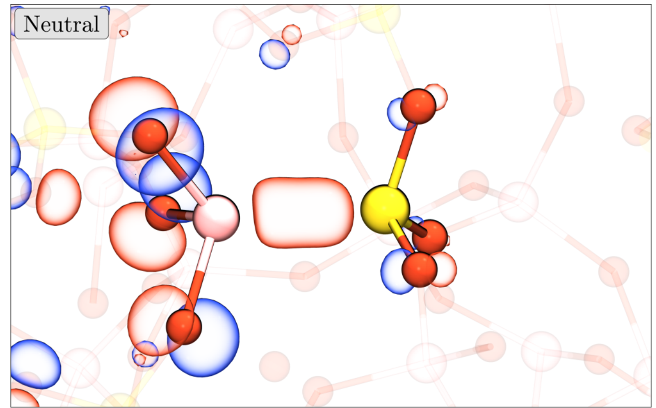

FIG. 2. Atomistic structure and highest occupied orbital of the neutral vacancy in $Si_xGe_{1-x}O_2$ where the Si content is 25%. The Si, Ge, and O atoms are represented by pink, yellow, and red spheres, respectively. The displayed vacancy is made of a Si and Ge atom. However, the vacancy had the same qualitative electronic and atomistic structure for all atom combinations. The orbital is occupied by two electrons and the isovalue of the orbital's surface is 0.05 eÅ^{-3}.

1. Neutral charge state

The optimized atomistic structures were qualitatively similar across all concentrations, an example of which is shown in Fig. 2. As is the case for the vacancy in pure a-SiO_2 and a-GeO_2, the highest occupied molecular orbital (HOMO) was a bonding orbital between the two atoms at the vacancy; however, some of the HOMO is delocalized in the p orbitals of nearby O atoms.

It was found that the quantitative behavior of the defect was defined not by the various concentrations of $Si_xGe_{1-x}O_2$, but rather by the atoms composing the vacancy. The bond length for a vacancy was found to be *2.51 Å, 2.41 Å*, and *2.45 Å* on average. Figure 3 in the Supplemental Material shows the distribution of the different bond lengths across all concentrations [49]. The vacancy bond length distribution was found to be extremely narrow, with a standard deviation of below 0.1 Å for all vacancy types. The bond lengths here are similar to those recently reported in the literature [32]; however, older studies report that the Ge-Ge dimer tends to be shorter than Si-Si [31]. The one-electron Kohn-Sham (KS) level was found to sit *0.53 eV, 0.76 eV,* and *0.61 eV* on average above the valence band, with a standard deviation no higher than 0.2 eV (see Fig. 6 of the Supplemental Material [49]).

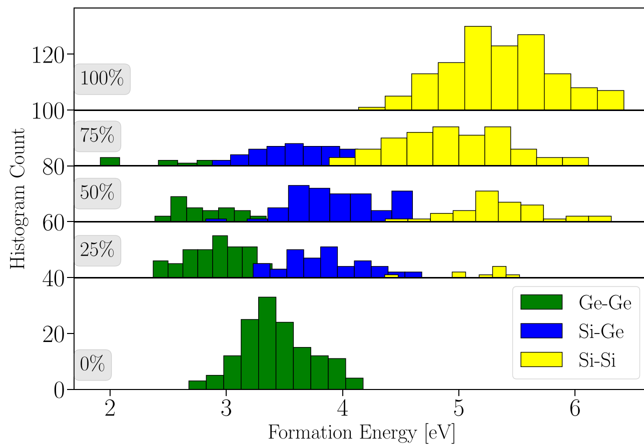

FIG. 3. Histograms of the neutral oxygen vacancy's formation energy in $Si_xGe_{1-x}O_2$ systems. The formation energies are decomposed by the atoms surrounding the vacancy, with green, yellow, and blue bars representing vacancies composed of Ge-Ge, Si-Si, or Si-Ge, respectively. From bottom to top, the rows represent 0%, 25%, 75%, and 100% Si concentration.

The formation energy of the neutral vacancy was calculated according to Eq. (1) and is shown in Fig. 3. The histogram is split into five rows, showing the various concentrations from 0% Si at the bottom up to 100% Si at the top. One can immediately see that the atoms surrounding the vacancy are the defining feature controlling the formation energy, which is otherwise very broad. The average formation energies were *3.1 eV, 5.4 eV*, and *3.8 eV*. As was found for Ge-doped SiO_2 [32], the Ge-Ge dimer formation energy is much lower than the other types, indicating that it would be more prevalent in the material. Although the neutral formation energies showed little dependence on concentration, it was found to be strongly affected by the distance between the atoms making up the vacancy. The relationship between the dimer length and the formation energy is shown in the top panel of Fig. 4. This is to be expected as a longer bond length is weaker and higher in energy, resulting in a higher formation energy.

2. Negative charge state

Starting from the optimized neutral vacancies, an electron was added to each configuration and their geometries were optimized. In a number of configurations (approximately 25% of the models), this resulted in the additional electron delocalizing at the bottom of the conduction band instead of getting trapped at the vacancy; such cases are not considered in the results.

However, the vast majority of electrons localized at the dimer, resulting in a negatively charged vacancy, which is depicted in Fig. 5. Qualitatively, the structure of the negatively charged vacancies was the same, regardless of the $Si_xGe_{1-x}O_2$ concentration or the atoms surrounding the vacancy, as was the case for its neutral analog. The dimer length increased relative to the neutral vacancy and the additional electron localized at the two atoms surrounding the vacancy as well as their neighbors, shown in the spin density in Fig. 5. The distances between the vacancy's atoms were *2.84 Å, 2.57 Å*, and *3.12 Å*. As was the case for the neutral state, the Ge-Ge dimer is longer than the Si-Si dimer. However, the Si-Ge dimer increases much more than the other dimers. Figure 4 in the Supplemental Material shows the distribution of bond lengths across all concentrations [49].

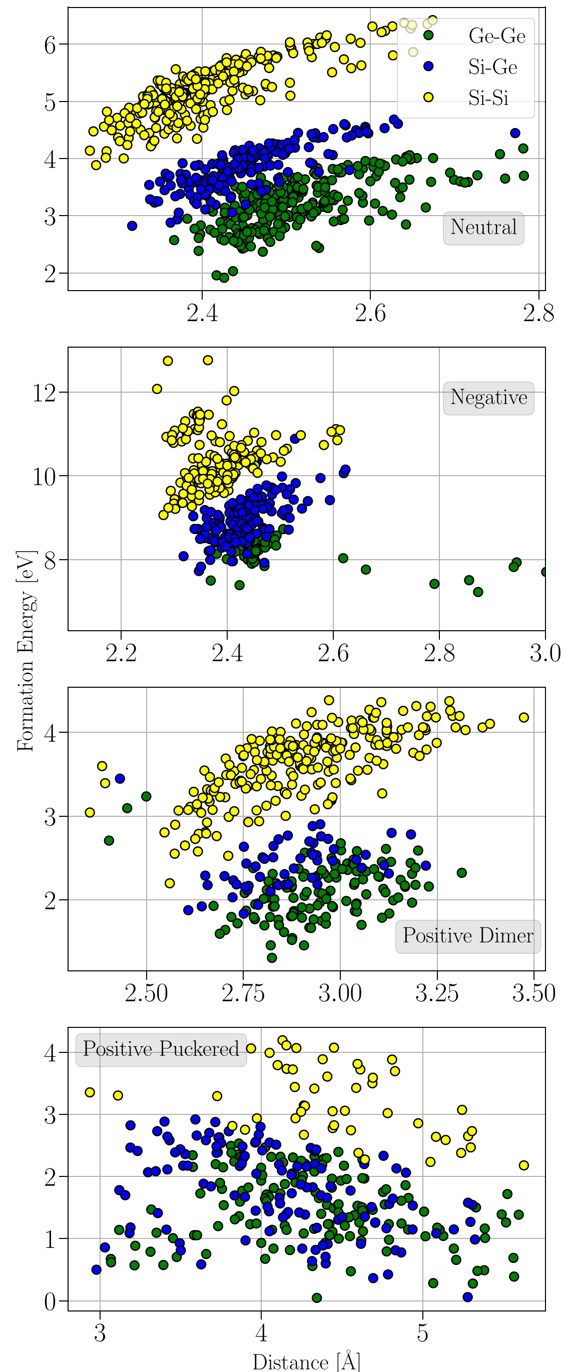

FIG. 4. Scatter plot of the oxygen vacancy's formation energy in $Si_xGe_{1-x}O_2$ against the distance of the atoms surrounding the vacancy. The panels show results for the neutral, negative, and positive (dimer and puckered) charge states. Green, yellow, and blue circles are vacancies composed of Ge-Ge, Si-Si, and Si-Ge dimers, respectively.

The one-electron KS levels of the additional electron measured from the top of the relevant $Si_xGe_{1-x}O_2$ valence band were *3.81 eV, 5.7 eV*, and *3.82 eV*. The negative Ge-Ge con-

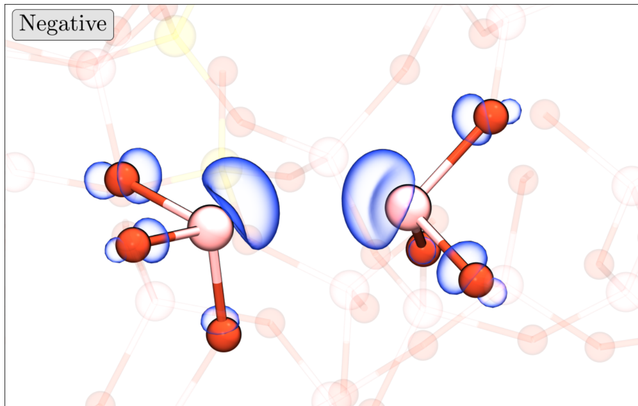

FIG. 5. The spin density and geometry of the negatively charged Ge-Ge vacancy in $Si_xGe_{1-x}O_2$ where the Si content is 50%. The atoms around the vacancy are both Ge, but the structure is qualitatively similar regardless of the atoms surrounding the vacancy. The color scheme is the same as that in Fig. 2. The orbital isosurface's isovalue was set to 0.05 eÅ^{-3}.

figuration is clearly more stable than its Si counterpart, whose KS level is rather high. In fact, trapping an electron at the Si-Si vacancy compared to the other dimers was more unlikely to happen as the Ge content increased due to the KS level being closer to the bottom of the conduction band. In those cases, the electron preferentially delocalizes into a band state. The distribution of KS levels for the negative vacancy can be found in Fig. 7 of the Supplemental Material [49].

The negative vacancy's formation energies are shown in the second panel of Fig. 4 with respect to the dimer length. The formation energy was calculated with the Fermi level chosen to be at the top of the $Si_xGe_{1-x}O_2$ valence band, hence the higher values. Similar to the neutral vacancy, its negative counterpart shows a dependence of its formation energy on the dimer distance, regardless of the atoms involved. The $Si_xGe_{1-x}O_2$ concentration also had no discernible effect on the calculated formation energies.

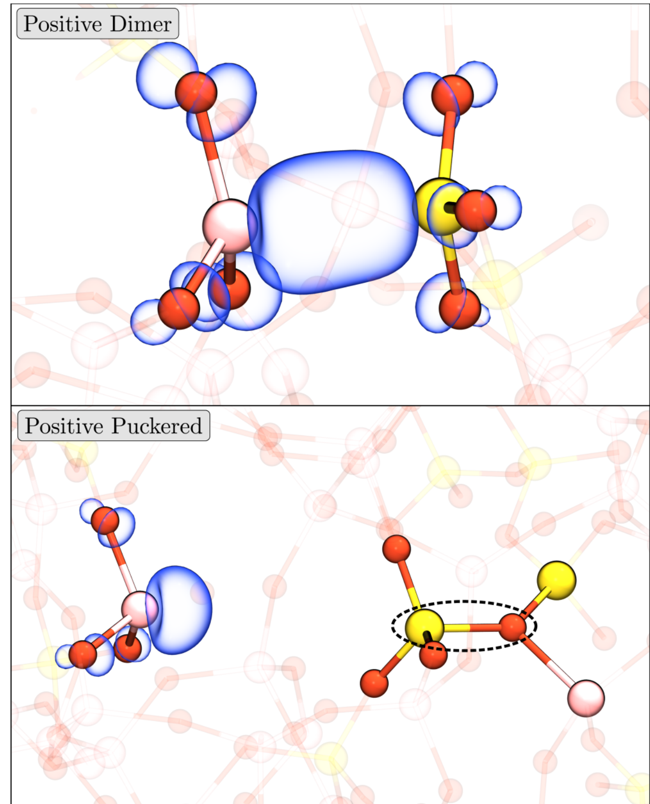

FIG. 6. Atomistic structure and spin density of the positively charged vacancy in $Si_xGe_{1-x}O_2$ where the Si content is 50%. The color scheme can be found in Fig. 2. The positive vacancy has two configurations: the dimer (top panel) and the puckered (bottom panel) configurations. For both configurations, an Si and a Ge atom was visualized. We note, however, that the atomistic and electronic structures are qualitatively similar regardless of the atoms around the vacancy. The interaction between the Si and a back oxygen in the puckered configuration is highlighted by a dashed ellipsis. Note that this is not a covalent bond, but rather an electrostatic interaction between the positively charged Si and the negatively charged O. The isovalue of both orbital's surface was set to 0.05 eÅ^{-3}.

3. Positive charge states

The positively charged vacancy was calculated by adding a hole into the neutral vacancy, followed by an optimization of the structure's energy. Similar to the neutral and negative vacancies, the positively charged systems were qualitatively similar regardless of Si concentration. However, unlike the other charge states, the positive vacancies showed (meta)stable states: the dimer and puckered configurations [23]. The dimer configuration shows shorter distances between the surrounding atoms of *2.92 Å, 2.88 Å*, and *2.79 Å*, respectively. Their puckered counterparts have distances of *4.11 Å*, *3.91 Å*, and *4.12 Å*, respectively. The Si-Si dimer length is close to the 2.9 Å calculated in the literature [27]. The distributions of vacancy bond lengths can be found in Fig. 5 of the Supplemental Material [49].

For the dimer configuration, the distance increases compared to the neutral state as there is now one fewer electron in its bonding orbital, resulting in a weaker bond. The dimer introduces a singly occupied KS orbital in the band gap, which sits *0.65 eV, 0.71 eV*, and *0.47 eV* above the corresponding valence band. The distribution of Kohn-Sham levels can be seen in Fig. 8 of the Supplemental Material [49]. The puckered configuration's electronic structure is qualitatively different, with a dangling bond on one Si while the other has moved through the plane of its neighbors [23]. It can be easily identified as it is more positively charged than the other equivalent atoms in the system. The bottom panel of Fig. 6 shows an example of the puckered structure, where the electron is in a dangling bond on the Ge atom on the left side. The positively charged Si ion forms a favorable weak interaction with an oxygen due to this relaxation. We note that when the atoms surrounding the vacancy are Si-Ge and the system is in the puckered configuration, the dangling bond was always localized on the Ge ion, while the hole is on the Si ion, similar to the structure shown in the bottom panel of Fig. 6.

The formation energies of the positively charged vacancies are rather varied, reflecting the two possible configurations. The bottom two panels of Fig. 4 shows how the forma-

tion energy varies with the distance between the two ions surrounding the vacancy. The two configurations, dimer and puckered, were distinguished using their spin moments, shown in Figs. 9 and 10 of the Supplemental Material [49]. As was the case for the negative vacancy, the Fermi level is set to the top of the valence band of the relevant $Si_xGe_{1-x}O_2$ system. The dimer configurations show a clear positive correlation with distance, with the formation energy increasing rapidly as the interatomic distance increases since the binding energy provided by the Si-Si bond reduces substantially with distance. The puckered configuration, instead, shows a very weak negative correlation, if any at all. Curiously, the atoms surrounding the vacancy showed a difference in the proportion of the dimer to puckered configurations. For Si-Si atoms, 71% were dimers and 29% were puckered. The Ge-Ge dimers had a rather different proportion, with 35% preferring to be in the dimer configuration and 65% in the puckered. The Si-Ge configurations sat very much in the middle of these two, with 57% dimer configurations and 43% puckered.

IV. DISCUSSION AND CONCLUSIONS

The oxygen vacancy was modeled in various concentrations of a-$Si_xGe_{1-x}O_2$. Similar to previous studies, it was found that the structural and electronic properties of defect-free $Si_xGe_{1-x}O_2$ varied rather smoothly with Ge content [48,50,51]. Although the effect of a rapidly changing band gap for low concentrations was seen previously [48], we explain this change as a transition from a molecular orbital to a band theory model. The oxygen vacancy was found to be a qualitatively similar defect across all values of the concentration x in $Si_xGe_{1-x}O_2$. This is an extension to the fact that Si-Si vacancies are qualitatively similar across α-quartz, a-SiO_2, and a-GeO_2. Remarkably, the vacancy showed similar properties that are independent of concentration when grouped by atoms making up the vacancy. The Ge-Ge dimer had the lowest formation energies across all the systems studied. Along similar lines, previous studies showed that the Si-Ge vacancies in Ge-doped SiO_2 had a lower formation energy than a Si-Si vacancy. [32]. Further optical absorption calculations on Ge-doped SiO_2 showed that the occupied states of the neutral oxygen vacancy participate in multiple transitions [34]. Curiously, the use of the GW formalism resulted in higher formation energies. In our study, we find an average formation energy of 3.8 eV for the Si-Ge vacancy, while a previous study showed a value of 3.97 eV. As previously mentioned, optimizing the amount of HFX would change the band gap as well as increase the defect state's energy. The lower formation energy of the Ge-Ge vacancy can be correlated to the lower Ge-O bond energy (3.3 eV) from chemical measurements making it easier to break those bonds than the Si-O bonds (4.7 eV) [52]. Indeed, experimental results show that the vacancy concentration is much higher in pure GeO_2 relative to SiO_2 [53].

The charged vacancies were found to behave similarly to their a-SiO_2 counterparts [27,35]. The negatively charged vacancies only showed one type of configuration, where an additional electron was delocalized over the two atoms surrounding the vacancy. Due to the proximity of the negatively charged state to the conduction band, not all vacancies were found to trap an electron. The decreasing band gap as a function of Ge concentration in $Si_xGe_{1-x}O_2$ means that defects in Ge-rich $Si_xGe_{1-x}O_2$ were the most affected by this, as their unoccupied Kohn-Sham levels sit closer to the edge of the conduction band. On the other hand, the positively charged vacancies showed the two distinct, well-known configurations, namely, the dimer and puckered [27,31]. They result in a broad distribution of formation energies and distances between the atoms surrounding the vacancies. Our analysis shows that the formation energies for the neutral, negative, and positive dimer configurations show a fairly strong positive correlation with the bond length (see Fig. 4). The positive puckered configuration instead has a weak negative correlation, perhaps due to its particularly strong relaxation. Previous simulations have correlated the Si-Si bond distance of neutral vacancies with the energy of the system as well as its forma-

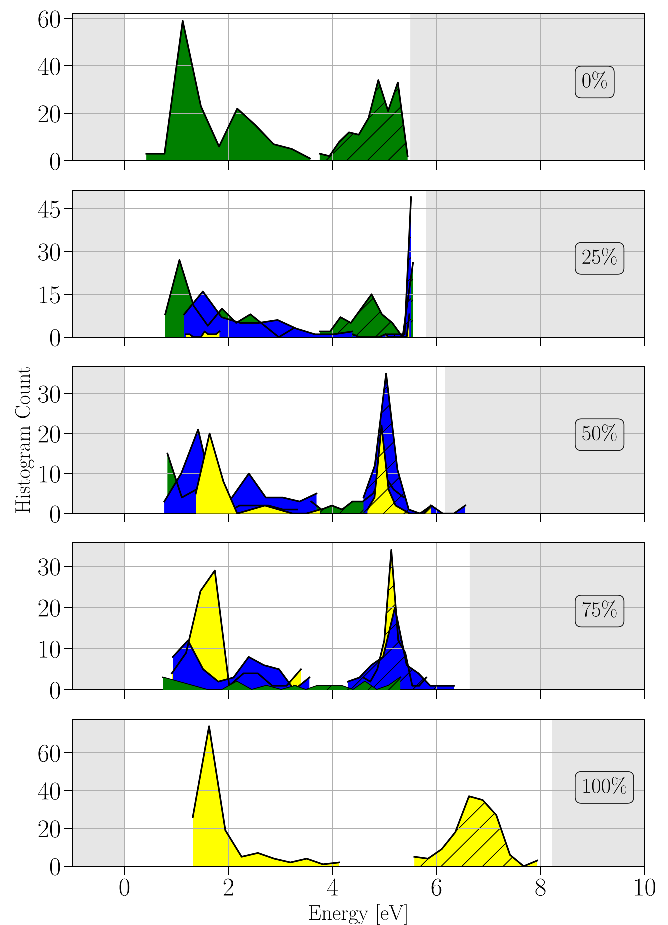

FIG. 7. Histogram of the vacancy's charge transition levels in varying concentrations, indicated in the gray boxes, of Si in $Si_xGe_{1-x}O_2$. The levels are referenced to the top of the $Si_xGe_{1-x}O_2$ valence band for the relevant concentration. The green histograms correspond to Ge-Ge, yellow to Si-Si, and blue to Si-Ge vacancies. The (+/0) transition levels are the curves with a solid fill, while the curves with a hatched fill are the (0/−) transition levels. The shaded regions represent band edges: below 0 eV is the valence band edge, while the regions above 0 eV are the concentration-dependent conduction band edges as indicated.

tion energy [54,55]. It is not, however, the only correlation that can be made, and indeed previous studies have shown a strong correlation with the strain of the vacancy and its formation energy [56]. For the negative and positive charge states, particularly for the puckered configurations, it could perhaps be better correlated with the formation energy than simply using the distance between the vacancy's atoms.

We note that for both the positive and negative configurations, these are unlikely to be the only stable configurations. One could imagine that these vacancies can undergo similar conversion mechanisms, such as from the vacancy into the so-called Ge(2) center, a 2-coordinated Ge point defect that has been calculated in Ge-doped a-SiO_2 and a-GeO_2 [33]. We note that the charged configurations obtained in this work are certainly not the global minima of their respective charge states. In our calculations, a charge was added to the optimized neutral configuration. As could be seen in the positive charge state, two distinct metastable configurations were possible. However, simply adding a charge means that a lower-energy state could be missed. A Monte Carlo sampling approach could be used to unambiguously identify which geometric configuration is truly the lowest-energy state for a given charge state. However, this is beyond the scope of this work.

The corresponding distribution of thermodynamic charge transition levels, which are important in the context of device reliability since they determine the charge trapping behavior of defects, is shown in Fig. 7. One can see that the contribution from the different types of vacancies results in an extremely wide charge transition level distribution which covers a large proportion of the band gap. It has been reported that reliability issues such as bias temperature instability (BTI) and hot carrier degradation (HCD) are less severe in SiGe devices than in their Si counterparts [13–15]. By using single-defect spectroscopy to identify single traps under BTI conditions in combination with a statistical analysis, one can identify a band of defect energies that contribute to BTI. A $SiGe/Si/SiO_2/HfO_2$ model stack was used to investigate BTI in SiGe devices and it was found that the extracted defect energies were extremely similar to those from pure Si devices [57]. Measurements and calculations suggest that BTI in Si-based devices is caused by defects containing a 3-coordinated Si, such as the hydroxyl E′ center or the hydrogen bridge [58]. The calculations of oxygen vacancies presented here show that they are unlikely to be involved in systems that have either mixed or pure $Si_xGe_{1-x}O_2$. Further calculations of 3-coordinated Si defects in $Si_xGe_{1-x}O_2$ could be used to help understand their role in reliability issues.

Perhaps surprisingly, it was shown that the concentration itself does not have such a large effect on the vacancy's properties. However, the atoms making up the vacancy were found to be the feature that defines their properties. By splitting the vacancies up in this way, one can identify distributions for the vacancy's properties which are close to a normal distribution. Further calculations using these structures, such as optical absorption or electron resonance spectra, could be used to unambiguously identify vacancy-related issues in hybrid $Si_xGe_{1-x}O_2$ systems.

ACKNOWLEDGMENTS

The authors would like to acknowledge support from the Vienna Scientific Cluster for providing computer resources on the Austrian high-performance clusters VSC3 and VSC4. They would like to thank the Austrian Science Fund (FWF) under Project No. P31204-N30. This project has received funding from the European Union's Horizon 2020 research and innovation programme under Grant Agreement No. 871813, within the framework of the project Modeling Unconventional Nanoscaled Device FABrication (MUNDFAB). This work was supported by the Ministry of Science and Higher Education of the Russian Federation under Grant No. 075-15-2020-790. For stimulating discussions on the characterization and physics of SiGe devices, the authors would like to thank V. V. Afanas'ev and M. Houssa.

[1] R. Soref, Silicon **2**, 1 (2010).
[2] J. T. Clemens, Bell Labs Tech. J. **2**, 76 (1997).
[3] K. Kim, J. Y. Choi, T. Kim, S. H. Cho, and H. J. Chung, Nature (London) **479**, 338 (2011).
[4] A. L. Lewandowski, P. Schlexer, S. Tosoni, L. Gura, P. Marschalik, C. Büchner, H. Burrall, K. M. Burson, W. D. Schneider, G. Pacchioni, and M. Heyde, J. Phys. Chem. C **123**, 7889 (2019).
[5] D. A. Coucheron, M. Fokine, N. Patil, D. W. Breiby, O. T. Buset, N. Healy, A. C. Peacock, T. Hawkins, M. Jones, J. Ballato, and U. J. Gibson, Nat. Commun. **7**, 13265 (2016).
[6] K. Sasan, A. Lange, T. D. Yee, N. Dudukovic, D. T. Nguyen, M. A. Johnson, O. D. Herrera, J. H. Yoo, A. M. Sawvel, M. E. Ellis, C. M. Mah, R. Ryerson, L. L. Wong, T. Suratwala, J. F. Destino, and R. Dylla-Spears, ACS Appl. Mater. Interfaces **12**, 6736 (2020).
[7] S. Girard, J. Kuhnhenn, A. Gusarov, B. Brichard, M. V. Uffelen, Y. Ouerdane, A. Boukenter, and C. Marcandella, IEEE Trans. Nucl. Sci. **60**, 2015 (2013).
[8] D. J. Paul, Adv. Mater. **11**, 191 (1999).
[9] M. Jech, A.-M. El-Sayed, S. Tyaginov, A. L. Shluger, and T. Grasser, Phys. Rev. B **100**, 195302 (2019).
[10] M. Jech, A.-M. El-Sayed, S. Tyaginov, D. Waldhör, F. Bouakline, P. Saalfrank, D. Jabs, C. Jungemann, M. Waltl, and T. Grasser, Phys. Rev. Appl. **16**, 014026 (2021).
[11] S. Firstov, S. Alyshev, V. Khopin, M. Melkumov, A. Guryanov, and E. Dianov, Opt. Express **23**, 19226 (2015).
[12] S. Bandyopadhyay, J. Canning, P. Biswas, M. Stevenson, and K. Dasgupta, Opt. Express **19**, 1198 (2011).
[13] M. Waltl, G. Rzepa, A. Grill, W. Goes, J. Franco, B. Kaczer, L. Witters, J. Mitard, N. Horiguchi, and T. Grasser, IEEE Trans. Electron Devices **64**, 2092 (2017).
[14] M. Waltl, G. Rzepa, A. Grill, W. Goes, J. Franco, B. Kaczer, L. Witters, J. Mitard, N. Horiguchi, and T. Grasser, IEEE Trans. Electron Devices **64**, 2099 (2017).
[15] S. Tyaginov, A.-M. El-Sayed, A. Makarov, A. Chasin, H. Arimura, M. Vandemaele, M. Jech, E. Capogreco, L. Witters, A. Grill, A. De Keersgieter, G. Eneman, D. Linten, and B. Kaczer, in *2019 IEEE International Electron Devices Meeting (IEDM)* (IEEE, Piscataway, NJ, 2019), pp. 21.3.1–21.3.4.

[16] R. A. Weeks, J. Appl. Phys. **27**, 1376 (1956).
[17] G. D. Watkins and J. W. Corbett, Phys. Rev. **134**, A1359 (1964).
[18] F. J. Feigl and J. H. Anderson, J. Phys. Chem. Solids **31**, 575 (1970).
[19] F. J. Feigl, W. B. Fowler, and K. L. Yip, Solid State Commun. **14**, 225 (1974).
[20] J. Isoya and J. A. Weil, J. Chem. Phys. **74**, 5436 (1981).
[21] J. K. Rudra and W. B. Fowler, Phys. Rev. B **35**, 8223 (1987).
[22] N. Lopez, F. Illas, and G. Pacchioni, J. Phys. Chem. B **104**, 5471 (2000).
[23] M. Boero, A. Pasquarello, J. Sarnthein, and R. Car, Phys. Rev. Lett. **78**, 887 (1997).
[24] V. B. Sulimov, P. V. Sushko, A. H. Edwards, A. L. Shluger, and A. M. Stoneham, Phys. Rev. B **66**, 024108 (2002).
[25] B. Tuttle and S. T. Pantelides, Phys. Rev. B **79**, 115206 (2009).
[26] S. T. Pantelides, Z. Y. Lu, C. Nicklaw, T. Bakos, S. N. Rashkeev, D. M. Fleetwood, and R. D. Schrimpf, J. Non-Cryst. Solids **354**, 217 (2008).
[27] S. Mukhopadhyay, P. V. Sushko, A. M. Stoneham, and A. L. Shluger, Phys. Rev. B **70**, 195203 (2004).
[28] G. Buscarino, S. Agnello, and F. M. Gelardi, Phys. Rev. B **73**, 045208 (2006).
[29] D. L. Griscom, J. Non-Cryst. Solids **357**, 1945 (2011).
[30] G. Pacchioni and C. Mazzeo, Phys. Rev. B **62**, 5452 (2000).
[31] T. Tamura, G. H. Lu, R. Yamamoto, and M. Kohyama, Phys. Rev. B **69**, 195204 (2004).
[32] N. Richard, S. Girard, L. Martin-Samos, V. Cuny, A. Boukenter, Y. Ouerdane, and J. P. Meunier, J. Non-Cryst. Solids **357**, 1994 (2011).
[33] L. Giacomazzi, L. Martin-Samos, A. Boukenter, Y. Ouerdane, S. Girard, A. Alessi, S. D. Gironcoli, and N. Richard, Nanotechnology **28**, 195202 (2017).
[34] N. Richard, L. Martin-Samos, S. Girard, A. Ruini, A. Boukenter, Y. Ouerdane, and J. P. Meunier, J. Phys.: Condens. Matter **25**, 335502 (2013).
[35] M. S. Munde, D. Z. Gao, and A. L. Shluger, J. Phys.: Condens. Matter **29**, 245701 (2017).
[36] A.-M. El-Sayed, M. B. Watkins, V. V. Afanas'ev, and A. L. Shluger, Phys. Rev. B **89**, 125201 (2014).
[37] M. Micoulaut, L. Cormier, and G. S. Henderson, J. Phys.: Condens. Matter **18**, R753 (2006).
[38] T. D. Kühne, M. Iannuzzi, M. Del Ben, V. V. Rybkin, P. Seewald, F. Stein, T. Laino, R. Z. Khaliullin, O. Schütt, F. Schiffmann *et al.*, J. Chem. Phys. **152**, 194103 (2020).
[39] G. Lippert, J. Hütter, and M. Parrinello, Mol. Phys. **92**, 477 (1997).
[40] J. VandeVondele and J. Hutter, J. Chem. Phys. **127**, 114105 (2007).
[41] M. Guidon, J. Hutter, and J. VandeVondele, J. Chem. Theory Comput. **5**, 3010 (2009).
[42] M. Guidon, J. Hutter, and J. VandeVondele, J. Chem. Theory Comput. **6**, 2348 (2010).
[43] C. G. Van De Walle and J. Neugebauer, J. Appl. Phys. **95**, 3851 (2004).
[44] S. Lany and A. Zunger, Modell. Simul. Mater. Sci. Eng. **17**, 084002 (2009).
[45] H.-P. Komsa, T. T. Rantala, and A. Pasquarello, Phys. Rev. B **86**, 045112 (2012).
[46] C. Freysoldt, J. Neugebauer, and C. G. V. de Walle, Phys. Status Solidi B **248**, 1067 (2011).
[47] T. R. Durrant, S. T. Murphy, M. B. Watkins, and A. L. Shluger, J. Chem. Phys. **149**, 024103 (2018).
[48] K. Baral, P. Adhikari, and W. Y. Ching, J. Am. Ceram. Soc. **99**, 3677 (2016).
[49] See Supplemental Material at http://link.aps.org/supplemental/10.1103/PhysRevMaterials.6.125002 for further calculated properties of $Si_xGe_{1-x}O_2$.
[50] F. López-Gejo, M. Busso, and C. Pisani, J. Phys. Chem. B **107**, 2944 (2003).
[51] B. Walker, C. C. Dharmawardhana, N. Dari, P. Rulis, and W. Y. Ching, J. Non-Cryst. Solids **428**, 176 (2015).
[52] Y.-R. Luo, *Comprehensive Handbook of Chemical Bond Energies*, 1st ed. (CRC Press, Boca Raton, FL, 2007).
[53] H. Hosono, Y. Abe, D. L. Kinser, R. A. Weeks, K. Muta, and H. Kawazoe, Phys. Rev. B **46**, 11445 (1992).
[54] A. C. Pineda and S. P. Karna, J. Phys. Chem. A **104**, 4699 (2000).
[55] S. Mukhopadhyay, P. V. Sushko, A. M. Stoneham, and A. L. Shluger, Phys. Rev. B **71**, 235204 (2005).
[56] L. Martin-Samos, Y. Limoge, J.-P. Crocombette, G. Roma, N. Richard, E. Anglada, and E. Artacho, Phys. Rev. B **71**, 014116 (2005).
[57] G. Rzepa, J. Franco, B. O. Sullivan, A. Subirats, M. Simicic, G. Hellings, P. Weckx, M. Jech, T. Knobloch, M. Waltl, P. J. Roussel, D. Linten, B. Kaczer, and T. Grasser, Microelectron. Reliab. **85**, 49 (2018).
[58] A.-M. El-Sayed, M. B. Watkins, T. Grasser, V. V. Afanas'ev, and A. L. Shluger, Phys. Rev. Lett. **114**, 115503 (2015).